Corrosion-Fatigue of Ti-6Al-4V Coupons Manufactured by Directed Energy Deposition

D.G. Hattingh[1,4], S. Botha[1], D. Bernard[4], M.N. James[1,3] and A. du Plessis[1,2]

[1] Department of Mechanical Engineering, Nelson Mandela University, Private Bag X6011, Port Elizabeth 6000, South Africa

[2] Research group 3D Innovation, Stellenbosch University, Stellenbosch, 7602, South Africa

[3] School of Engineering, Computing and Mathematics, University of Plymouth, Drake Circus, Devon PL4 8AA, England, UK

[4] eNtsa, Nelson Mandela University, Private Bag X6011, Port Elizabeth 6000, South Africa

Corresponding Author: D.G. Hattingh

Corresponding Author Contact Information: danie.hattingh@mandela.ac.za

Nelson Mandela University - North Campus M-Block, Room M038
Gardham Avenue, Summerstrand, Port Elizabeth, 6000
South Africa

Abstract

Titanium is a versatile biocompatible metal that is desirable in additively manufactured medical implant devices. However, additively manufactured parts have particular microstructures, porosity, residual stress and surface conditions which can have a strong impact on fatigue performance. Implants have an added complexity from the saline operating environment and the associated impact on the safe design life. Equally, direct energy deposition induces a complex thermal history which, if not carefully controlled, can significantly alter the mechanical/material properties of the component. This study investigates the decrease in fatigue life, in an in-vitro body fluid simulation using Ringer's solution, observed in Ti-6Al-4V specimens extracted from coupons manufactured by directed energy deposition. An interrupted deposition strategy was employed to control build regularity, which appeared to influence certain mechanical properties, including corrosion fatigue life. An ≈50% decrease in fatigue life was observed in Ringer's solution at 6 Hz loading frequency, clearly important in designing implants.

Keywords: Directed energy deposition; Laser additive manufacturing; Interrupted build strategy; Ti-6Al-4V alloy; Corrosion fatigue

1. Introduction

Fatigue failures of medical implants are both undesirable and well documented [1,2]. The decrease in fatigue strength of implant materials when exposed to corrosion conditions is

equally well known [3,4]. There are, however, very few reports of in-vitro simulations of the effect of body fluids on the fatigue characteristics of implants manufactured by AM or directed energy deposition (DED) techniques [5,6]. Wegner et al investigated laser powder bed fusion magnesium alloy implants in an in-vitro environment, along with ultra-high molecular weight polyethylene (UHMWPE), and titanium implants. Their intention was to develop and demonstrate that an in-vitro test set-up reduced the time necessary to perform fatigue characterisation. Li et al, in contrast, investigated porous Ti-6Al-4V scaffolds manufactured with different pore sizes by electron beam melting, in order to assess cytocompatibility and osteointegration in vitro. There is a clear lack of data regarding the fatigue performance of metallic AM alloys in terms of manufacturing and loading parameters, and saline environment effects. Consequently, the present study investigated the rotating bend fatigue performance of Ti-6Al-4V specimens, manufactured by a DED technique, tested in either an atmospheric or a simulated body fluid environment.

In this initial study, the work focused on the influence of a simulated body fluid environment and the defect population in the DED specimens. The important influence of the wide range of surface roughness that would occur on the surface of geometrically complex biomedical implants was excluded, due to the limited time and scope available in the postgraduate research project. Surface roughness is a highly influential factor on fatigue life, and is subject to large sample-to-sample variation. The topics of surface roughness, porosity and residual stresses have recently been reviewed by Ye Chang et al in a review paper of their effect on the fatigue performance of AM metals [7]. In trying to understand the net effect of such influences on the fatigue life of biomedical components, it is the view of the authors that it is more effective to first study each effect separately, to establish basic relationships between influence and fatigue performance, before seeking to understand the interaction between these independent contributors to fatigue life in genuine biomedical components. Future work by the authors is planned to address this important issue.

Directed energy deposition (DED) is an important additive manufacturing (AM) process capable of producing fully dense metallic parts for industrial applications. It is a metal additive manufacturing process whereby metal is injected into a melt pool by wire or via blown powder, with the melt pool formed by either a laser, electron beam or electric arc. In this work, we investigate powder-blown laser-based DED. DED has advantages in the manufacturing of high-performance medical prostheses through rapid near-net shape production of parts with good mechanical properties. Reference [8] gives a comprehensive overview of the current state

of DED in terms of physical characteristics, defects, challenges and applications, and some key aspects of the process are briefly mentioned below. The properties of components produced by DED depend on several factors, including the technology used, the build environment atmosphere (vacuum or inert gas), process parameters and the rapid and repeated heating-cooling cycles that affect the microstructure and its related physical and mechanical properties [8]. The thermal history of DED-manufactured components or specimens controls the macrostructure and the microstructure, and they generally exhibit anisotropy in both microstructure and its associated mechanical properties. Defect population can be reduced through process optimisation, monitoring and feedback control.

DED manufacturing is based on a 3D computer-aided design model that is sliced into thin parallel layers, perpendicular to the selected build direction (commonly referred to as the z-direction) which the AM machine processes to manufacture the complex shaped part, as discussed by Azarniya et al [9] with particular reference to Ti-6Al-4V. As titanium alloys are highly reactive with oxygen and nitrogen, their DED processing requires an inert atmosphere (blown inert gas or inert chamber conditions). Post-processing is usually required to mitigate the effects of such issues as surface finish, microstructure, porosity, and residual stresses in AM components, which have an adverse effect on their long-term fatigue performance [7]. AM post-processing for Ti-6Al-4V components and their influence on fatigue properties is also discussed in detail by Azarniya et al [9].

Quantifying the fatigue performance of DED components and identifying process parameters that can be manipulated to provide improved fatigue performance is critical to achieving effective design and use as medical implants. Shamsaei et al [10] discuss fatigue resistance in Ti-6Al-4V components manufactured by direct laser deposition (DLD), which is an alternate name for DED. They pay particular attention to the important topic of process optimisation for enhanced mechanical properties, where significant work has already been performed in the development of process optimisation maps, e.g. [11,12]. Similar work has been previously published for other fabrication techniques where microstructural change and residual stresses are a concomitant effect of the process, e.g. friction stir welding [13,14]. However, Zhang et al [15] have noted that reducing the size and density of defects and improving the alloy performance for AM Ti-6Al-4V components is better addressed using post-processing heat treatment. They considered the evolution of microstructure and associated electrochemical properties in AM Ti-6Al-4V after the application of four different heat treatment methods. They observed that

variations in the amount of α and β phases in the titanium alloy were the main factors affecting the corrosion behaviour in Ringer's solution.

Although Ti-6Al-4V has excellent corrosion resistance in normal environments, due to its surface oxide film, other work has shown that the microstructural heterogeneity in the alloy, arising from fusion joining processes, causes corrosion fatigue in a simulated seawater environment, e.g. in 100 mm thick electron beam welded Ti-6Al-4V plate [16] and in 6 mm compact tension specimens of Ti-6Al-4V alloy specimens produced by selective laser melting (SLM) [17]. Equally, biofouling in marine environments is known to exacerbate corrosion issues with titanium alloys, as discussed in the state-of-the-art review by Yan et al [18]. The work has also shown that in common with fatigue processes more generally, crack initiation is often associated with the presence of stress concentrations at manufacturing or corrosion-induced defects [17], or microstructural boundaries [16]. The relationship between plastic strain accumulation, microstructural features such prior-β grain boundaries and α' laths, and the location of defects like voids and lack-of-fusion, and their impact on fatigue crack growth mechanisms were investigated in work using 1.5 mm thick single-edge notch specimens of Ti-6Al-4V [19]. The AM specimens were produced using powder bed fusion and direct metal laser melting, with high resolution digital image correlation and microstructural characterisation being used to examine microstructural effects on fatigue and fracture behaviour. Significant observations were that regions where the crack propagated along α' laths and deflected at prior-β grain boundaries were observed in all AM samples, regardless of build orientation; and that the fatigue crack also propagated towards voids on the surface. The authors also noted that the differences in microstructure between AM and conventionally manufactured Ti-6Al-4V led to differences in the plastic wake in the AM samples, which was asymmetric and unpredictable in its response to load changes. In turn, this then influenced the crack path, fatigue crack growth and the fatigue lifetime.

Crack initiation to a relatively small crack length of ~ 1 mm can take up to 90% of the fatigue life at low stress, long life situations, dropping to perhaps 10% at fatigue lives ~ 10^4 load cycles. Stress concentrators such as notches or defects also reduce the crack initiation life. Work by VanSickle et al [19] therefore noted the deleterious effect of voids and their grouping together on the fatigue life of AM Ti-6Al-4V, while Roach, Williamson and Zardiackas [20] tested smooth and notched specimens (K_t = 3.2) of Ti-6Al-4V in Ringer's solution at 37°C and 1 Hz. They observed that notched specimens showed a significant reduction in fatigue life compared with the smooth specimens but did not present data comparing their results with those obtained in

an air environment. It would therefore be expected that corrosion damage, such as pitting or crevice corrosion, would significantly shorten the time or number of load cycles necessary to initiate a crack. In the context of medical implant devices, it is therefore clearly important to characterise and understand corrosion damage and corrosion fatigue in DED Ti-6Al-4V alloys.

Corrosion fatigue is a time-dependent phenomenon and the test frequency will have a strong influence on its occurrence. This effect, however, is strongly alloy and microstructure dependent. In 5083-H131 aluminium alloy, for example, work by Bay et al [21] on the effect of sensitisation and loading frequency effect found that the acceleration in crack growth rate was strongly dependent on the degree of sensitisation, i.e. the grain boundary precipitation of the Mg-rich β phase (Al_3Mg_2) in alloys with more than ~ 3 wt% Mg, and on loading frequencies < 1 Hz. The frequency of 1 Hz has also been reported as a useful upper threshold figure for the onset of corrosion fatigue in other alloys [22,23]. However, work by Zavanelli et al [24] reported that tensile fatigue testing round bar specimens of both commercially pure titanium and Ti-6Al-4V in synthetic saliva showed a decrease in fatigue life, compared with an air environment, even at a test frequency of 10 Hz. The present study has investigated the rotating bend fatigue performance of Ti-6Al-4V specimens, manufactured by an interrupted DED technique, tested in either an atmospheric air at 50 Hz or in a simulated body fluid environment at 6 Hz.

This paper is structured into the following sections; Section 2 - Experimental Methods: that provides details of the specimens and their manufacturing process, and the fatigue testing in air and in Ringer's solution. Section 3 - Results and Discussion: that covers the experimental data and their interpretation, dealing with mechanical properties and microstructure in section 3.1, fatigue testing in section 3.2 and computed tomography data in section 3.3. Section 4 presents the conclusions from the study.

2. Experimental methods

2.1 Specimens

Specimens for tensile and fatigue testing were machined from Ti-6Al-4V coupons manufactured by DED using a TruLaser Robot 5020 laser cell (4 kW TruDisk 4001 Yb: YAG laser). Figure 1 schematically shows the AM titanium coupon and the positions along the z-direction where specimens were machined from it. The final minimum coupon dimensions were length 100 mm, width 10 mm and build height 41 mm. A total of 20 coupons were made in an inert argon environment on Grade 2 titanium baseplates, with the baseplate oxide layer being removed before starting the AM process, in order to provide improved adherence

between the first deposited layer and the baseplate. A three-stage multilayer interrupted build sequence was adopted with a layer thickness of approximately 1 mm. This interrupted build technique had been previously shown to assist in maintaining a vertical, parallel-sided coupon during the AM process. It involved removing the top 2.50 mm from the coupon after every 14 layers (equating to an average build height of 14.00 mm) until the z-direction height was approximately 40 mm. After each process interruption, the laser path was re-aligned with the machined surface of the coupon to ensure that coupon dimensional regularity was maintained.

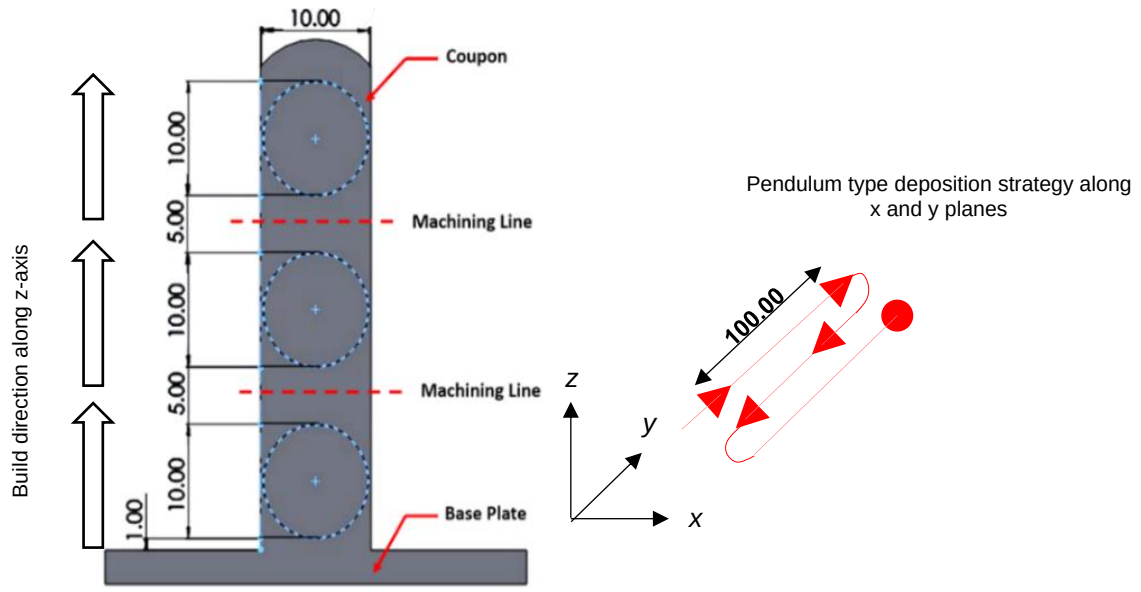

Figure 1 Diagram showing the coupon dimensions (mm), build direction and positions of the various specimens in the coupon.

Table 1 Summary of the DED process parameters used in this work

Parameter	
Laser Power (W)	1800
Scanning Speed (mm/sec)	12
Powder Mass Flow Rate (g/min)	9
Nozzle Angle Tilt (°)	4
Z-Step (mm)	1.10
Overlap (%)	40
Number of Layers/build stage	14

Table 1 gives the DED process parameters used, while both the powder carrier and argon gas flow rate were kept constant at 5 litre/min. These parameters were chosen as a result of earlier work carried out on the same alloy as part of another project, and were found to give an acceptable defect population and build geometry.

Three cylindrical specimens, 9 mm in diameter and 70 mm long were then machined from the coupons as indicated in Figure 1. These were subsequently machined into the hourglass shape used in the tensile and fatigue tests (see Figure 2).

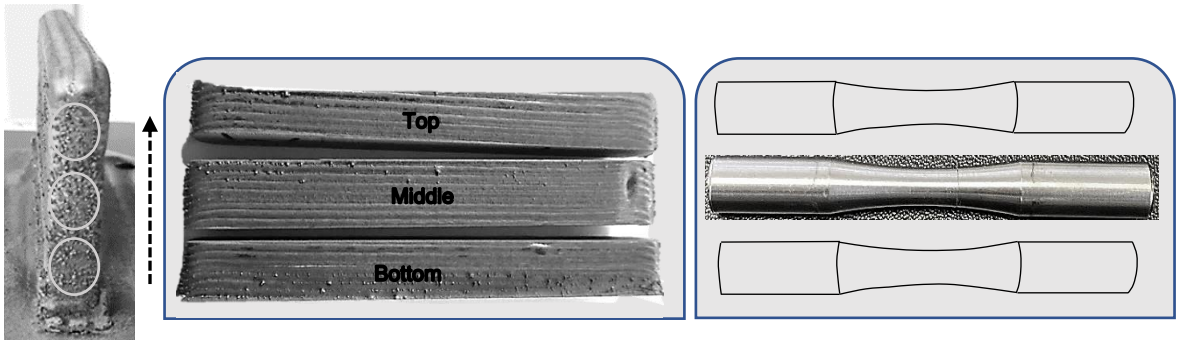

Figure 2 DED coupon showing the positions of the tensile and fatigue specimens.

Tensile specimens were manufactured and tested in accordance with ASTM-E8M [25] for static testing while the fatigue specimens followed the guidance in ASTM E466 [26]. All tests were performed on specimens in the as-built condition, i.e. without any post-processing heat treatment. Fatigue data for SLM Ti-6Al-4V has been published in the literature for both the as-manufactured state [27] and after post-processing by hot-isostatic pressing [28] with micro-pores and surface roughness being identified as the key factors controlling the fatigue strength [28,29]. In the present work, particular attention was directed towards controlling surface roughness to < 6 µm across the reduced test section on the fatigue specimens (as-machined). An Olympus DSX microscope was used to measure surface roughness (R_a) via optical interference [30]. The average calculated surface roughness values over the reduced diameter section where fatigue cracks initiated for the top, middle, and bottom positions in the AM coupons were 3.59 µm, 3.89 µm, and 3.54 µm respectively, resulting in an average R_a = 3.83 µm across all specimens.

2.2 Fatigue testing

Fatigue testing was performed on a Schenk rotating bend machine – PUNZ(Rapid) and a custom environmental cell was employed to maintain a constant flow of saline Ringer's solution onto the specimen (Figure 3a).

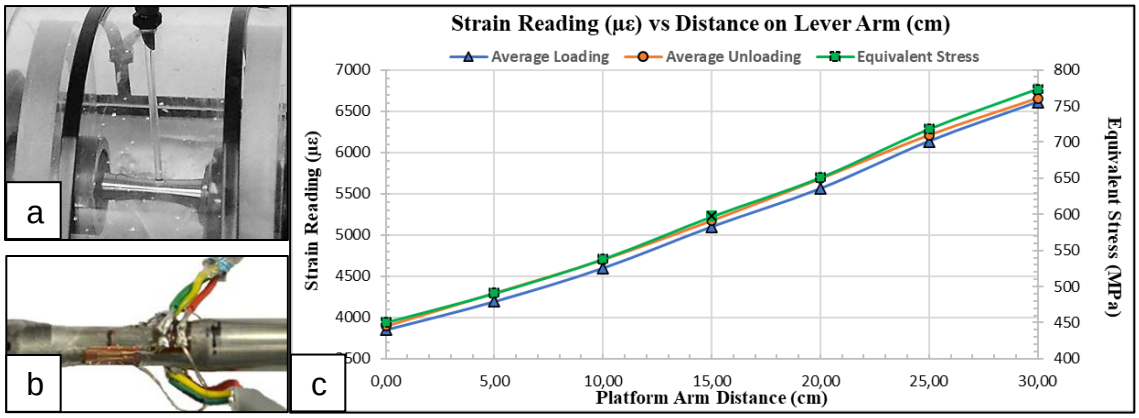

Figure 3 (a) Environmental cell showing the method of application of Ringer's saline solution
(b) Strain gauged specimen used for stress-strain calibration
(c) Stress-strain calibration curve for the lever arm of the fatigue test machine obtained via a strain gauged specimen

The Schenk testing machine operated in displacement control and setting fatigue stress levels on the specimens required a calibration curve to be developed between loading lever arm displacement and specimen strain. Standard equations were used to convert strain readings into stress values. Figure 3c shows the calibration curve along with an inset of the strain gauged specimen used to obtain it (Figure 3b). The continuing accuracy of this calibration curve was verified at regular intervals during fatigue testing using the strain gauged specimen and the calibration curve.

The frequency used in the saline fatigue tests was 6 Hz as Ringer's solution has previously been shown to cause corrosion fatigue in SLM Ti-6Al-4V at a test frequency of 10 Hz [17]. Leinenbach et al [31] also analysed data on human gait obtained by Bergmann et al during walking [32] to generate more realistic axial fatigue conditions in their work. They then used a triangular waveform with R = -1 and a frequency of 4.6 Hz. In the present study, testing at 6 Hz with a sinusoidal waveform required integrating a variable frequency drive (VFD) into the controls of the Schenk rotating bend test machine. Ringer's solution (pH = 7.0-7.4) is frequently used to simulate body fluids for in-vitro corrosion experiments because it is a solution of several salts dissolved in water that creates an isotonic solution relative to bodily fluids and it is used in clinical practice for replacing fluid loss and restoring a chemical balance

in cases of dehydration. Table 2 summarises the chemical composition of the Ringer's solution used in the present work. Table 2 also gives the measured density and pH of the solution used in the corrosion fatigue tests. For all tests, the room temperature and relative humidity (%) were recorded. The average room temperature was 18.2°C (±2°C) and the humidity was 62.3% (minimum 43% and maximum 82.5%). The saline environment would maintain this temperature.

Table 2 Chemical composition of Ringer's solution per litre of distilled water.

Chemical Compound	**Average (grams/litre)**
NaCl	8.797
KCl	0.432
$NaHCO_3$	0.209
$CaCl_2$	0.250
Measured Density	1.005 g/cm^3
Measured pH	7.013

Thirty-six fatigue specimens were sectioned from the twenty DED Ti-6Al-4V coupons along with nine tensile specimens. These were evenly divided between the three positions in the AM coupons, i.e., top, middle and bottom. Rotating bend fatigue tests with a fully reversed loading cycle (R = -1) were carried out with a maximum stress of either σ_{max} = 600 MPa or σ_{max} = 675 MPa. These stress levels were selected from preliminary S-N test data where run-out (N > 2 x 10^6 cycles) was achieved in an air environment at ≈ 525 MPa and represent lives between approximately 50,000 and 300,000 cycles with correspondingly acceptable test durations at 6 Hz. Any influences of a saline environment observed over this range of cyclic lives would be enhanced at longer fatigue lives. Tests were stopped via a displacement sensor that was triggered when a complete fracture of the specimen occurred. Nine fatigue specimens were tested at each stress range in each of the two environments (air and Ringer's solution).

3. Results and Discussion

3.1 Mechanical properties and microstructure

Data on tensile properties, surface roughness, microstructure, porosity density in the failure region using X-ray computed tomography, and fatigue life at the two applied stress levels were acquired from the specimens as a function of coupon position, and test environment. Figure 4

shows average UTS values and the strain to failure as a function of the three coupon positions. The two graphs show a trend with the middle position giving higher tensile strength and a lower strain to failure, although the observed decrease in failure strain is very much more significant than would be expected from the ≈ 10% increase in UTS at the middle position relative to the top position (5% relative to the bottom position). The average 0.2% proof stress values were 945 MPa (top), 1069 MPa (middle) and 996 MPa (bottom). This anomalous ductility and UTS values at the middle position in the coupon are believed to be likely to be a result of the interrupted build strategy.

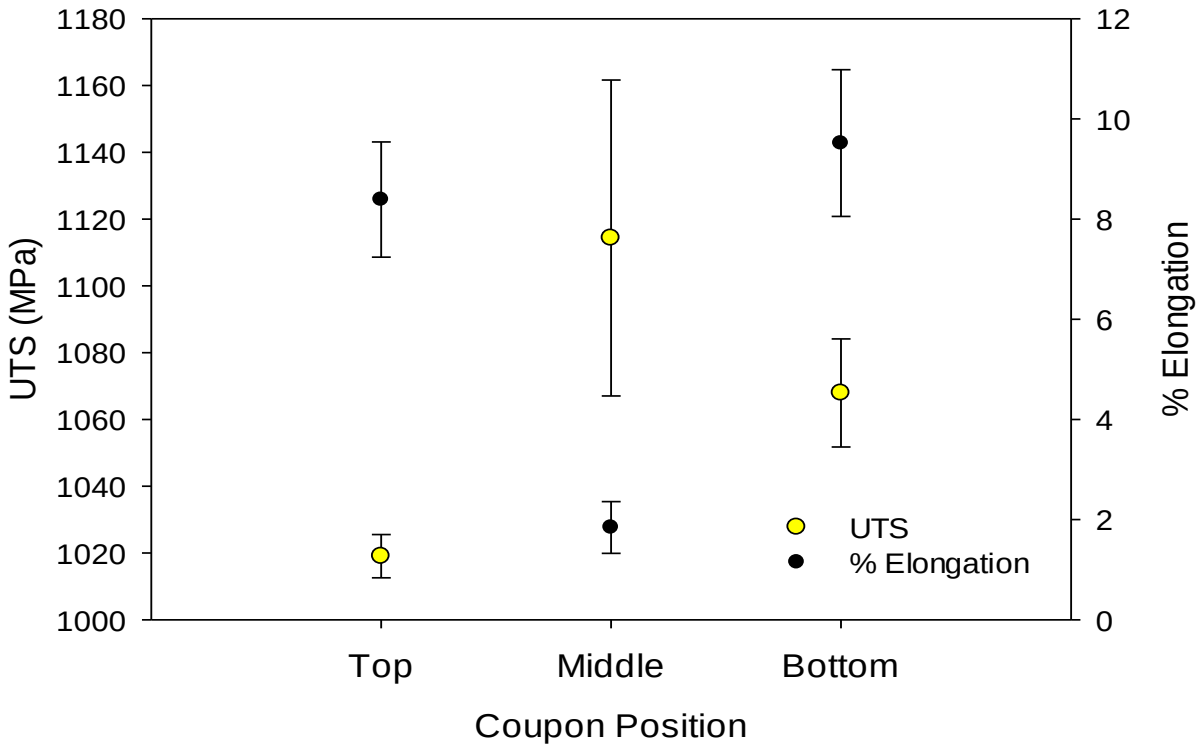

Figure 4 Ultimate tensile strength and average strain to failure versus coupon position (mean values with standard deviation shown for UTS values).

This interrupted build strategy represents a difference in thermal cycles between the bottom 14 mm of the coupon (three heating and cooling cycles), two cycles in the middle 14 mm and one in the top 13 mm. However, little discernible difference was observed in the microstructure at the three coupon positions (Figure 5). Independent of the specimen position in the coupon, all specimens had a fine α + β lamellar structure, in which a mixture of basket-weave and Widmanstätten structures was present. In Figure 5, the α and α′ phases are bright while the β

phase appears dark. The as-built microstructures are dominated by fine needle-shaped α′ martensite.

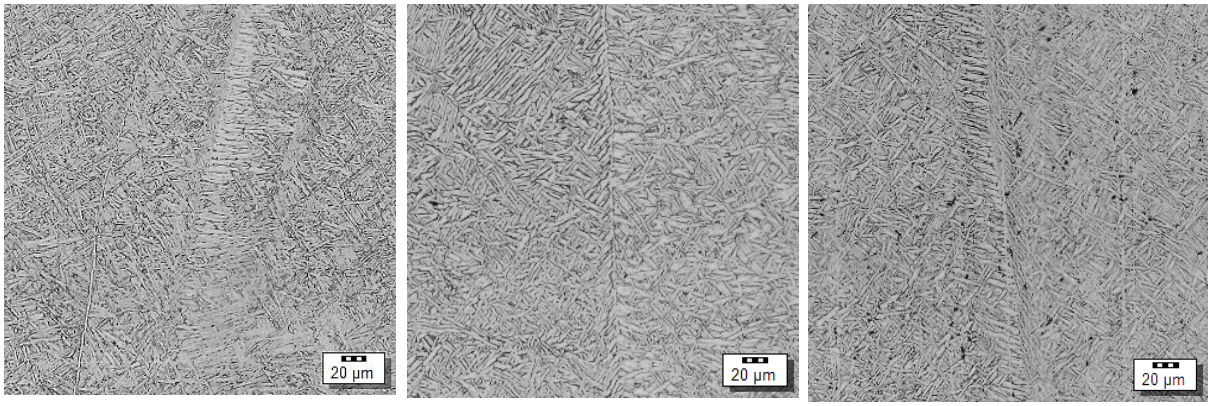

Figure 5 Micrograph of (a) bottom, (b) middle, and (c) top coupon specimens. The microstructure comprises a mixture of fine α + β lamellar basket-weave and Widmanstätten structures.

Vickers microhardness measurements were made on twelve specimens, four from each of the coupon extraction positions corresponding to build heights of 6 mm (Bottom), 21 mm (Middle) and 36 mm (Top). The specimens were randomly selected across the range of the available coupons. Four hardness indentations, at 1 mm spacing, were made across the width of the coupon, perpendicularly to its centreline on a sectioned specimen. A load of 500 gf was applied with a dwell time of 15 seconds. Figure 6 plots average hardness against coupon height measured at the centre of the specimens.

Average hardness values at the top, middle, and bottom coupon positions were 364 H_V, 393 H_V, and 375 H_V respectively and as expected this follows the same trend line seen in the UTS values (Figure 4). The bottom section of the coupon, which experienced three heating cycles in the interrupted build process shows a significantly smaller hardness range across the four specimens (17 H_V) compared to the middle (46 H_V) and top (42 H_V) coupon positions.

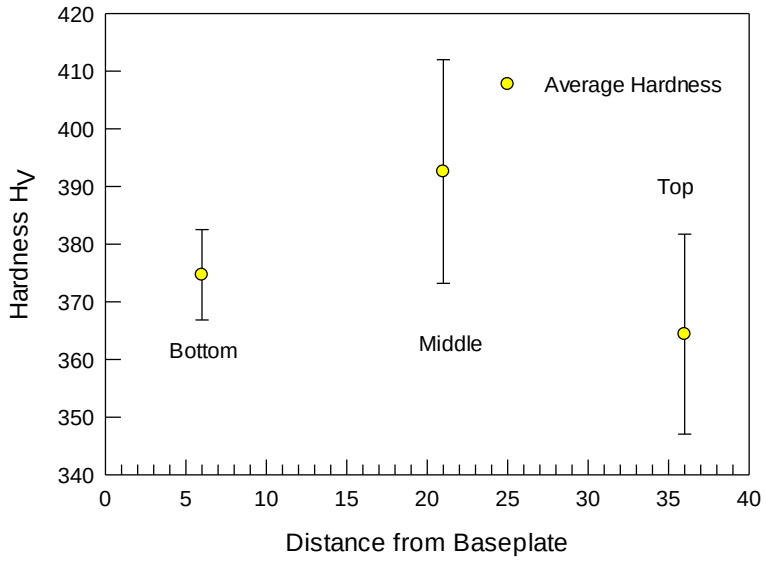

Figure 6 Average Vickers hardness measured as a function of distance from the baseplate.

3.2 Fatigue testing

Ten fatigue tests in air and eleven in the Ringer's solution were carried out at 600 MPa while for the 675 MPa stress level, nineteen fatigue tests were suitable for analysis (10 from air and 9 from Ringer's solution). The test frequency in air was set at 50 Hz, whilst for the corrosion fatigue tests, a reduced frequency of 6 Hz was used to ensure that there would be a corrosion influence on the fatigue life. This change in frequency would not be expected to cause any discernible intrinsic change in fatigue performance from crack tip heating, as exemplified in work performed on Ti-6Al-4V by Morrissey et al at higher frequencies of 70 Hz and 400 Hz, where a minor increase in fatigue strength was observed [33]. The only effect of frequency expected in the current work would arise from the change in environment. The complete set of fatigue data is shown in Figure 7 (numerical data given in Table 3) as a function of coupon position and stress level, while Figure 8 plots the average life at each coupon position as a function of stress level and environment (numerical average coupon data given in Table 4).

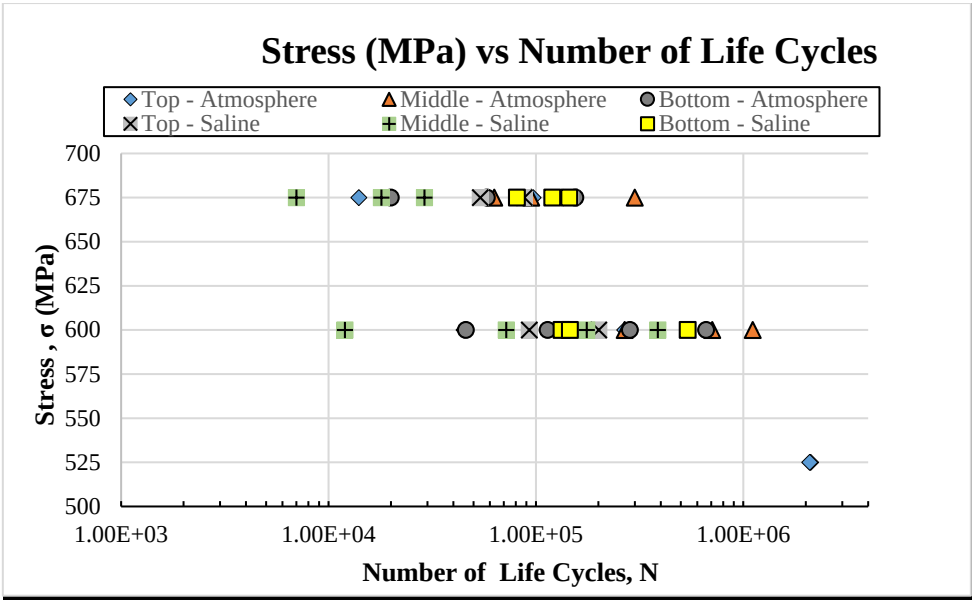

Figure 7 Stress-life data for all tests as a function of coupon position and test environment.

The average fatigue data present a slightly mixed picture when considering the individual coupon positions and their relative performance in air or Ringer's solution, as indicated by the relevant data at the bottom of Table 3. For instance, the top coupon position shows a 71% increase in fatigue life in Ringer's solution at 600 MPa and a reduction of 24% at 675 MPa, compared with air, whilst the middle and bottom positions show a reduction in fatigue life in all cases in the saline Ringer's solution. The reduction was seen at 600 MPa at the bottom position, however, is very much less (1.4%) than seen in the other results. An important consideration when evaluating the fatigue life at the individual extraction positions is the influence of the relatively small number of samples available at each extraction position. Although most of the fatigue initiation was surface related, two specimens exhibited subsurface crack initiation. These subsurface crack initiation sites are shown in the fractographs given in Figure 9, and these particular tests gave much-reduced fatigue lives compared with the other data.

Table 3 Fatigue life data as a function of stress, specimen position and environment with the extracted average fatigue life for each stress, position and test environment.

Stress Level	Label		Environ-ment	Life Cycles (N)	Stress Level	Label		Environ-ment	Life Cycles (N)
600 MPa	S	Top	Air	4.50E+04	675 MPa	AG	Top	Air	9.70E+04
		Middle	Air	2.68E+05			Middle	Air	9.50E+04
		Bottom	Air	4.60E+04			Bottom	Air	2.00E+04
	AE	Top	Air	1.38E+05		V	Top	Air	1.40E+04
		Middle	Air	7.09E+05			Middle	Air	3.00E+05
		Bottom	Air	6.62E+05			Bottom	Air	1.55E+05
	O	Top	Air	2.68E+05		X	Top	Air	5.80E+04
		Middle	Air	1.11E+06			Middle	Air	6.30E+04
		Bottom	Air	1.14E+05			Bottom	Air	6.31E+05
	AA	Bottom	Air	2.84E+05		Y	Bottom	Air	5.80E+04
	Z	Middle	Saline	7.20E+04			Top	Saline	8.80E+04
	AH	Top	Saline	9.30E+04		U	Middle	Saline	1.80E+04
		Middle	Saline	1.76E+05			Bottom	Saline	1.20E+05
	T	Top	Saline	2.01E+05		W	Top	Saline	5.40E+04
		Middle	Saline	1.46E+05			Middle	Saline	7.00E+03
		Bottom	Saline	1.33E+05			Bottom	Saline	1.45E+05
	R	Top	Saline	4.70E+04		P	Top	Saline	1.47E+05
		Middle	Saline	1.20E+04			Middle	Saline	2.90E+04
		Bottom	Saline	5.40E+05			Bottom	Saline	8.10E+04
	Q	Middle	Saline	3.87E+05	525 MPa	Q	Top	Air	2.11E+06
		Bottom	Saline	1.46E+05		Y	Top	Air	2.09E+06

Average fatigue life for samples as a function of coupon position and environment

	Top		Middle		Bottom	
	Air	Saline	Air	Saline	Air	Saline
600 MPa	1.50E+05	1.14E+05	6.96E+05	1.59E+05	2.77E+05	2.73E+05
675 MPa	5.63E+04	9.63E+04	1.53E+05	1.80E+04	2.16E+05	1.15E+05

Table 4 Average coupon fatigue life for all tests in air and in a saline environment.

Stress Level	**Average Fatigue Cycles** (All coupon positions)		**Decrease in Fatigue life in Saline Environment**	
	Air	**Saline**	**Cycles**	**% Reduction***
600 MPa	3.74E+05	1.82E+05	1.92E+04	51%
675 MPa	1.42E+05	7.66E+04	6.51E+04	46%
* % shift was calculated as Saline Life/Air Life				

If, however, the data for all three positions are averaged (see Table 4), a fairly uniform reduction in life is seen at both stress levels in Ringer's solution. The data in Table 4 and Figure 8 indicate that in fatigue, at 6 Hz, the presence of a saline environment leads to a ≈ 50% reduction in component life for Ti-6Al-4V coupons manufactured using laser DED with an interrupted build strategy. In other work on corrosion fatigue of Ti-6Al-4V alloys, Baragatti and Arcieri [34] tested 3 mm thick specimens of rolled and heat-treated plate in a 3.5% NaCl environment at 10 Hz and R = 0.1. They observed a reduction of about 20% in the fatigue life in the corrosive environment. A greater corrosion influence would be expected for specimens of an AM alloy tested in Ringer's solution at 6 Hz and R = -1, as used in the present work.

3.3 Computed tomography

In the present work, the primary focus was on the influence on fatigue life of the in-vitro Ringer's solution, with a secondary interest in any influence of the interrupted build technique on the fatigue data. However, the somewhat contradictory fatigue results seen in the individual coupon positions as a function of stress level prompted an X-ray computed tomography (CT) investigation of the porosity and other potential defects through-thickness in the region of the specimens where the fatigue cracks initiated. X-ray CT is often applied in the evaluation of porosity in additively manufactured materials [35,36]. In this work, specimens were scanned using a General Electric Vtomex 240, with 150 kV and 130 µA, at a voxel size of 20 µm. Porosity evaluation was performed using the workflow described in reference [37]. Eight specimens were selected for this examination, with this selection comprising samples from all three coupon positions, that had been fatigued at both stress levels and that gave fatigue lives across the whole range from 7.0 x 10^3 cycles to 1.11 x 10^6 cycles. The specimens are identified in Table 5 and they include the two specimens that showed subsurface crack initiation.

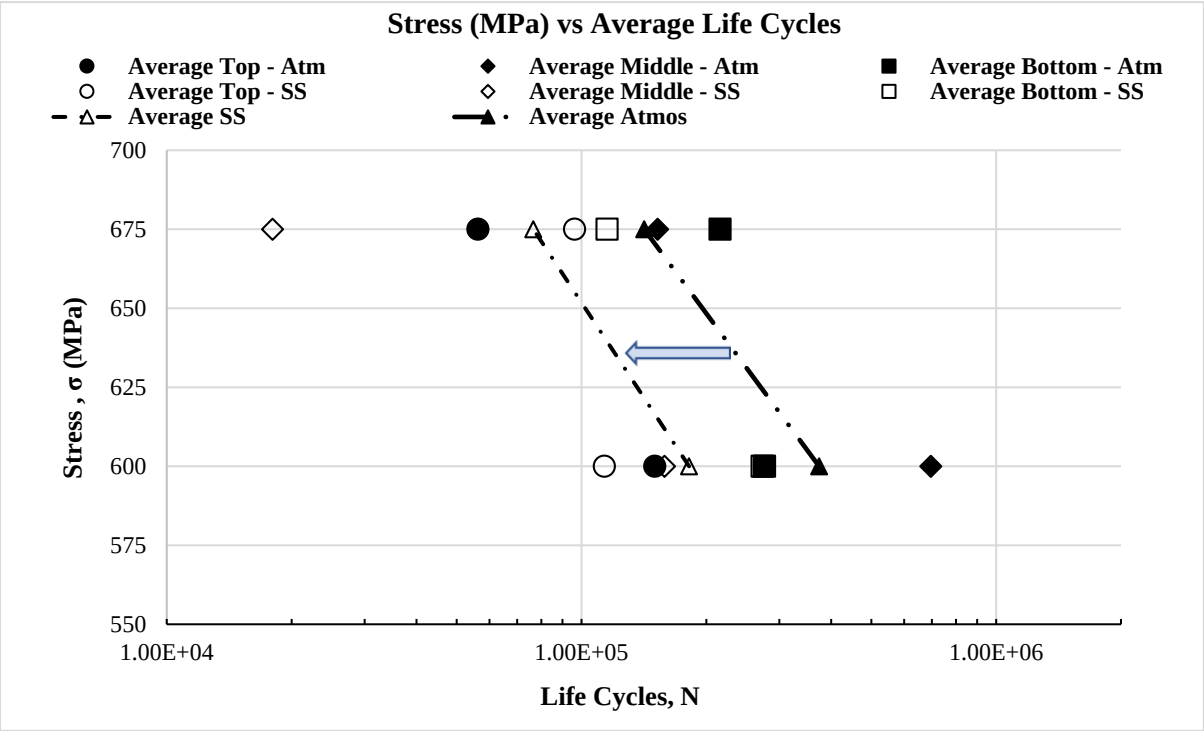

Figure 8 Reduction in fatigue life of AM Ti-6Al-4V specimens when tested in Ringer's solution. Data points represent the average life as a function of coupon position and test environment. The two dotted lines are average plots of fatigue life for all positions in air and Ringer's solution.

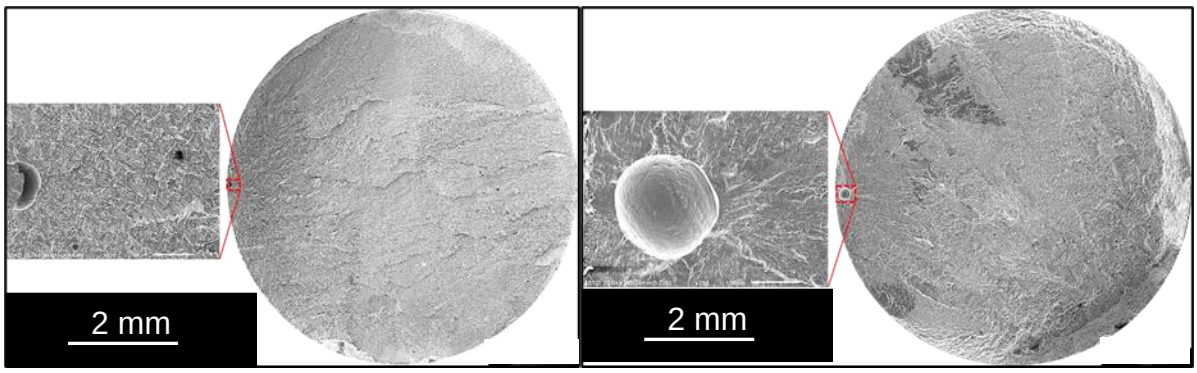

Figure 9 SEM fractographs showing (a) Middle coupon specimen after testing at 675 MPa in Ringer's solution (N_f = 7.0 x 10^3 cycles) and (b) Top coupon specimen after testing at 675 MPa in air (N_f = 1.4 x 10^4 cycles).

Table 5 Fatigue specimens used for X-Ray computed tomography.

Sample ID	Extraction Position	Test Environment	Life Cycles (N)	Stress Applied (MPa)	Test Frequency (Hz)	Description
S	Bottom	ATM	4,600E+04	600	50	Low life
O	Middle	ATM	1,110E+06	600	50	High Life
V	Top	ATM	1,400E+04	675	50	Low life
X	Bottom	ATM	6,310E+05	675	50	High Life
AH	Bottom	SS	1,700E+04	600	6	Low life
T	Top	SS	2,010E+05	600	6	High Life
W	Middle	SS	7,000E+03	675	5	Low life
P	Top	SS	1,470E+05	675	5	High Life

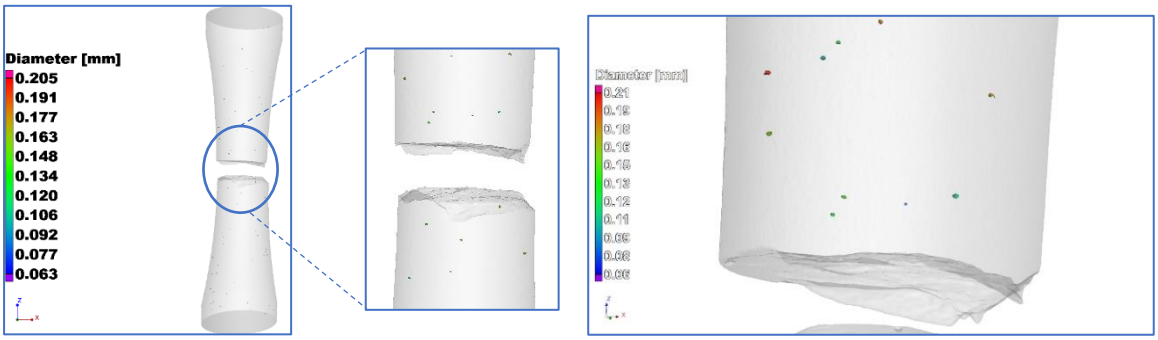

Figure 10 X-ray tomography image of specimen V, cut from the top of the coupon and having a low fatigue life.

The intention in this part of the work was twofold: firstly to determine whether the porosity in these specimens resulting from their manufacturing process was low enough that they would be representative of well-made implants and, secondly, to explore the possibility that porosity might be linked with thermal cycles, microstructure, and hence with fatigue life. Figure 10 shows an illustration of the area scanned around the fracture plane in the selected specimens and gives a coloured scale for the various sizes of porosity found to be present. The X-ray CT porosity data for all eight specimens is presented in Figure 11 which identifies the position in the DED coupon that the specimens were derived from, the test environment and the applied stress amplitude. The two specimens that showed subsurface crack initiation are identified in the figure with asterisks. In terms of the manufacturing quality of the DED coupons, the

average measured porosity across all eight samples was 0.0019% with a range from 0.0013% to 0.027%. This porosity range in the samples is exceptionally low, with higher levels often being reported in metal AM processes [38-40].

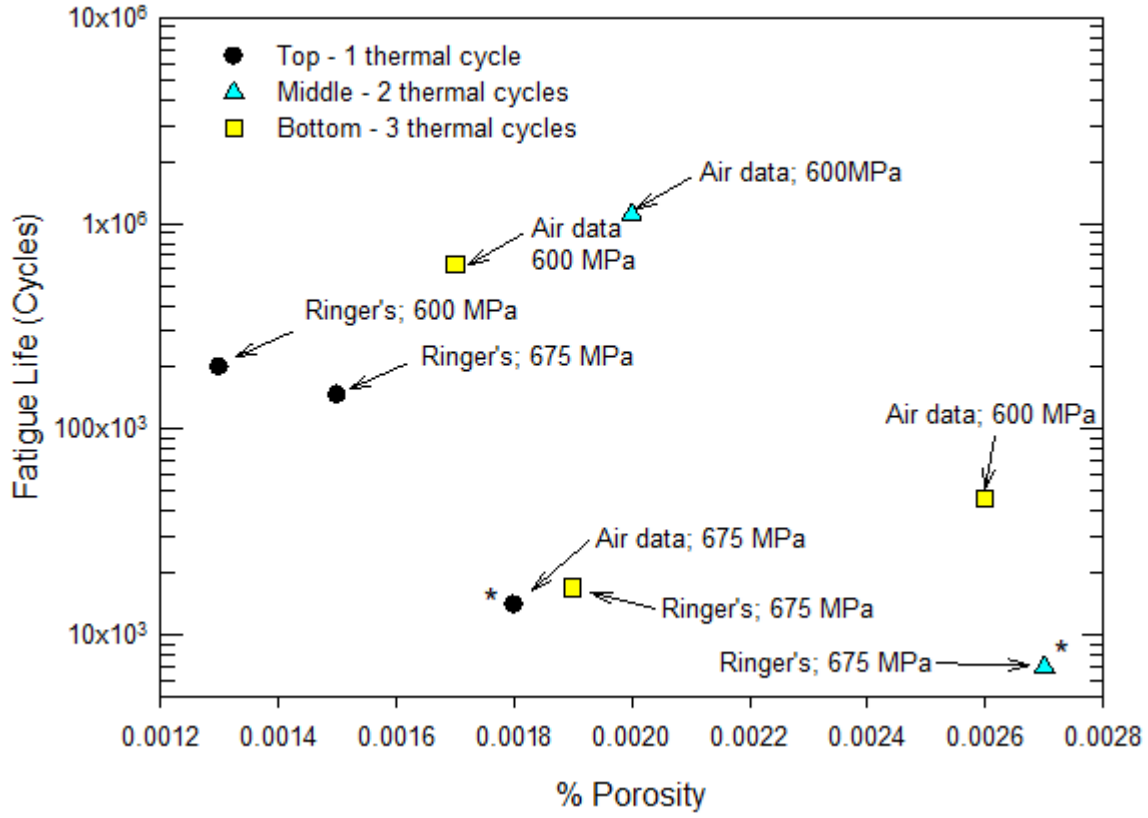

Figure 11 X-ray tomography porosity values plotted against fatigue life (N_f) identifying the environment and stress amplitude in each case. The two data points with asterisks are the two specimens with subsurface crack initiation.

In terms of linking fatigue life with porosity, it had been expected that the two environments (air and Ringer's solution) would give different relationships between N_f and porosity level. In fact, while no clear trends can be identified in the limited set of data available, several useful observations can be made. Firstly, if the two data points for specimens with subsurface initiation are excluded from consideration, Ringer's solution shows a clear reduction in fatigue life at similar levels of porosity, compared with air. Secondly, for this interrupted build sequence, there does appear to be an influence on the fatigue life of specimen position in the DED coupon and hence of the number of thermal cycles. The interrupted build process allows better dimensional control of the coupon, but the influence of the thermal history on fatigue

life clearly requires further work to determine its effect on porosity and microstructure and to understand the interaction between these three parameters. In particular, there appears likely to be the possibility of corrosion fatigue life being changed through control of the heating and cooling cycles and this important aspect merits further investigation.

4. Conclusions

This work further emphasises the importance of the in-vitro simulation medium on the fatigue life of Ti-6Al-4V AM implants when tested at an appropriate test frequency based on actual human gait measurements. This study did not explicitly focus on clarifying the influence of interrupted build techniques on the mechanical properties as a function of height from the baseplate but has shown that there is an effect that warrants further investigation. The interrupted process most probably reduced residual stress effects, while the remelting of underlying materials during subsequent heating and cooling cycles acted as in-situ heat treatment, effectively closing pores and hence potentially contributing a more homogenous microstructure throughout the build height.

Although Ti-6Al-4V is known for its superior corrosion resistance in an air environment, this study has shown, in agreement with other published work, that rotating bend fatigue in Ringer's solution reduces fatigue life by around 50%, compared with an air environment. X-ray CT analysis of the regions near some of the fracture surfaces indicated that the DED fatigue specimens had porosity levels in the range of 0.0013% to 0.027%. A link between fatigue life and the thermal history used in the DED process, through the resulting microstructure and its associated level of porosity was observed in the X-ray CT data. Thus if the two data points for specimens with subsurface initiation are excluded from consideration, Ringer's solution shows a clear reduction in fatigue life at similar levels of porosity, compared with air. Equally, for this interrupted build sequence, there does appear to be an influence on the fatigue life of specimen position in the DED coupon and hence of the number of thermal cycles that reflects the interrupted build strategy used to assist in maintaining dimensional tolerances on the coupons. Further work is required to fully clarify this aspect.

Declaration of Competing Interest

The authors declare that they have no competing financial interests or personal relationships that could have influenced the work reported in this paper.

Statement on Conflicts of Interest

The are no conflicts of interest of which the authors are aware.

Author contribution statement

All authors contributed equally to this paper.

Acknowledgements

The authors acknowledge the financial support for this work from the South African Department of Science and Innovation via the Light Metals Development Network program.

Highlights

- Interrupted build strategy
- In-situ heat treatment from build strategy
- Influence on fatigue life of in-vitro simulation medium
- X-ray CT data shows link between fatigue life and thermal history

References

1. Gatto A, Iuliano L, Atzeni E, Minetola P, Salmi A. Dental Failure Analysis: The Need of a Comprehensive Failure Classification. *Procedia CIRP*. 2017;62:429-434.
2. Halvorson TL, Cook SD, Brinker MR, Thomas KA, Sandborn PM. Failure analysis of retrieved cemented total knee prostheses. *Clinical Materials.* 1989;4(4):329-341.
3. Li L, Li C-Q, Mahmoodian M, Shi W. Corrosion induced degradation of fatigue strength of steel in service for 128 years. *Structures.* 2020;23:415-424.
4. Merot P, Morel F, Gallegos Mayorga L, Pessard E, Buttin P, Baffie T. Observations on the influence of process and corrosion related defects on the fatigue strength of 316L stainless steel manufactured by Laser Powder Bed Fusion (L-PBF). *International Journal of Fatigue.* 2021:106552.
5. Wegner N, Scholz R, Kotzem D, Barrientos MM, Walther F. Mechanical in vitro fatigue testing of implant materials and components using advanced characterization techniques. *Journal of Biomedical Materials Research.* 2021;110(4):898-909.
6. Li G, Wang L, Pan W, et al. In vitro and in vivo study of additive manufactured porous Ti6Al4V scaffolds for repairing bone defects. *Scientific Reports.* 2016;6(1):34072.
7. Ye C, Zhang C, Zhao J, Dong Y. Effects of Post-processing on the Surface Finish, Porosity, Residual Stresses, and Fatigue Performance of Additive Manufactured Metals: A Review. *Journal of Materials Engineering and Performance.* 2021;30(9):6407-6425.
8. Svetlizky D, Das M, Zheng B, et al. Directed energy deposition (DED) additive manufacturing: Physical characteristics, defects, challenges and applications. *Materials Today.* 2021.
9. Azarniya A, Colera XG, Mirzaali MJ, et al. Additive manufacturing of Ti–6Al–4V parts through laser metal deposition (LMD): Process, microstructure, and mechanical properties. *Journal of Alloys and Compounds.* 2019;804:163-191.

10. Shamsaei N, Yadollahi A, Bian L, Thompson SM. An overview of Direct Laser Deposition for additive manufacturing; Part II: Mechanical behavior, process parameter optimization and control. *Additive Manufacturing.* 2015;8:12-35.
11. Liu M, Kumar A, Bukkapatnam S, Kuttolamadom M. A Review of the Anomalies in Directed Energy Deposition (DED) Processes & Potential Solutions - Part Quality & Defects. *Procedia Manufacturing.* 2021;53:507-518.
12. Vasinonta A, Beuth JL, Griffith ML. A process map for consistent build conditions in the solid freeform fabrication of thin-walled structures. *Journal of Manufacturing Science and Engineering, Transactions of the ASME.* 2001;123(4):615-622.
13. Blignault C, Hattingh DG, James MN. Optimizing Friction Stir Welding via Statistical Design of Tool Geometry and Process Parameters. *Journal of Materials Engineering and Performance.* 2012;21(6):927-935.
14. Lombard H, Hattingh DG, Steuwer A, James MN. Optimising FSW process parameters to minimise defects and maximise fatigue life in 5083-H321 aluminium alloy. *Engineering Fracture Mechanics.* 2008;75(3):341-354.
15. Zhang Y, Feng L, Zhang T, Xu H, Li J. Heat treatment of additively manufactured Ti-6Al-4V alloy: Microstructure and electrochemical properties. *Journal of Alloys and Compounds.* 2021;888:161602.
16. Zeng CY, Zhang YP, Hu JL, et al. The role of microstructure on corrosion fatigue behavior of thick-plate Ti–6Al–4V joint via vacuum electron beam welding. *Vacuum.* 2020;182:109714.
17. Jesus JS, Borrego LP, Ferreira JAM, Costa JD, Capela C. Fatigue crack growth under corrosive environments of Ti-6Al-4V specimens produced by SLM. *Engineering Failure Analysis.* 2020;118:104852.
18. Yan S, Song G-L, Li Z, et al. A state-of-the-art review on passivation and biofouling of Ti and its alloys in marine environments. *Journal of Materials Science & Technology.* 2018;34(3):421-435.
19. VanSickle R, Foehring D, Chew HB, Lambros J. Microstructure effects on fatigue crack growth in additively manufactured Ti–6Al–4V. *Materials Science and Engineering: A.* 2020;795:139993.
20. Roach MD, Williamson RS, Zardiackas LD. A corrosion fatigue evaluation of implant grade titanium alloys. *Dental Materials.* 2011;27(Supplement 1):e71.
21. Bay RM, Schrock DJ, Akman AM, Bland LG, Thodla R, Locke JS. The effect of sensitization and fatigue loading frequency on corrosion fatigue of AA5083-H131. *International Journal of Fatigue.* 2019;124:1-9.
22. Barsom JM. Corrosion-fatigue crack propagation below KIscc. *Engineering Fracture Mechanics.* 1971;3(1):15-25.
23. Knop M, Heath J, Sterjovski Z, Lynch SP. Effects of cycle frequency on corrosion-fatigue crack growth in cathodically protected high-strength steels. *Procedia Engineering.* 2010;2(1):1243-1252.
24. Zavanelli RA, Pessanha Henriques GE, Ferreira I, de Almeida Rollo JMD. Corrosion-fatigue life of commercially pure titanium and Ti-6Al-4V alloys in different storage environments. *The Journal of Prosthetic Dentistry.* 2000;84(3):274-279.
25. ASTM. E8-13a: Standard Test Methods for Tension Testing of Metallic Materials. In. PA: ASTM International; 2013:28.
26. ASTM. E466-15: Standard practice for conducting force controlled constant amplitude axial fatigue tests of metallic materials. In. PA: ASTM International; 2021:6.
27. Chan KS, Koike M, Mason RL, Okabe T. Fatigue Life of Titanium Alloys Fabricated by Additive Layer Manufacturing Techniques for Dental Implants. *Metallurgical and Materials Transactions A.* 2013;44(2):1010-1022.

28. Leuders S, Thöne M, Riemer A, et al. On the mechanical behaviour of titanium alloy TiAl6V4 manufactured by selective laser melting: Fatigue resistance and crack growth performance. *International Journal of Fatigue.* 2013;48:300-307.
29. Nakatani M, Masuo H, Tanaka Y, Murakami Y. Effect of Surface Roughness on Fatigue Strength of Ti-6Al-4V Alloy Manufactured by Additive Manufacturing. *Procedia Structural Integrity.* 2019;19:294-301.
30. Kandpal HC, Mehta DS, Vaishya JS. Simple method for measurement of surface roughness using spectral interferometry. *Optics and Lasers in Engineering.* 2000;34(3):139-148.
31. Leinenbach C, Schwilling B, Eifler D. Cyclic deformation behaviour and fatigue induced surface damage of titanium alloys in simulated physiological media. *Materials Science and Engineering: C.* 2005;25(3):321-329.
32. Bergmann G, Deuretzbacher G, Heller M, et al. Hip contact forces and gait patterns from routine activities. *Journal of Biomechanics.* 2001;34(7):859-871.
33. Morrissey RJ, McDowell DL, Nicholas T. Frequency and stress ratio effects in high cycle fatigue of Ti-6Al-4V. *International Journal of Fatigue.* 1999;21(7):679-685.
34. Baragetti S, Arcieri EV. Corrosion fatigue behavior of Ti-6Al-4 V: Chemical and mechanical driving forces. *International Journal of Fatigue.* 2018;112:301-307.
35. Thompson A, Maskery I, Leach RK. X-ray computed tomography for additive manufacturing: a review. *Measurement Science and Technology.* 2016;27(7):072001.
36. du Plessis A. YI, Yadroitsava I., Le Roux S.G. X-Ray Microcomputed Tomography in Additive Manufacturing: A Review of the Current Technology and Applications. *3D Printing and Additive Manufacturing.* 2018;5(3):227-247.
37. du Plessis A, Sperling P, Beerlink A, du Preez WB, le Roux SG. Standard method for microCT-based additive manufacturing quality control 4: Metal powder analysis. *MethodsX.* 2018;5:1336-1345.
38. Sanaei N, Fatemi A. Defects in additive manufactured metals and their effect on fatigue performance: A state-of-the-art review. *Progress in Materials Science.* 2021;117:100724.
39. Sanaei N, Fatemi A, Phan N. Defect characteristics and analysis of their variability in metal L-PBF additive manufacturing. *Materials & Design.* 2019;182:108091.
40. du Plessis A. Effects of process parameters on porosity in laser powder bed fusion revealed by X-ray tomography. *Additive Manufacturing.* 2019;30:100871.